Phonon transport on two-dimensional graphene/boron nitride superlattices

Taishan Zhu and Elif Ertekin*

Department of Mechanical Science and Engineering, 1206 West Green Street, University of Illinois at Urbana-Champaign, Urbana, Illinois 61820, USA

(Received 12 September 2014; revised manuscript received 2 November 2014; published 26 November 2014)

Using nonequilibrium molecular dynamics and lattice dynamics, we investigate phonon conduction on two-dimensional graphene/boron nitride superlattices with varying periods and interface structures. As the period of superlattice increases to a critical value near 5 nm the lattice thermal conductivity drops sharply to a minimum, and beyond that it smoothly increases with the period. We show that the minimum in the thermal conductivity arises from a competition between lattice dispersion and anharmonic effects such as interface scattering. The initial reduction of thermal conductivity can partially be accounted for by harmonic wave effects induced by interfacial modulation, such as the opening of phononic band gaps and reduction of group velocity. Beyond the minimum, reduced inelastic interface scattering is responsible for the recovery. The overall range of thermal conductivity exhibited by the superlattices is substantially reduced with respect to the parent materials. A universal scaling of the thermal conductivity with total superlattice length is found, suggesting that the critical period is independent of total length and that long-wavelength phonons are dominant carriers. Furthermore, we demonstrate the ultrasensitivity of thermal conductivity to interfacial defects and superlattice periodicity disorder.

DOI: 10.1103/PhysRevB.90.195209 PACS number(s): 05.60.−k, 63.20.−e, 66.70.−f, 68.65.Cd

I. INTRODUCTION

Understanding the role of nanostructuring on lattice thermal transport is a key challenge with several practical applications. For instance, as thermal emissions continue to spike globally [1], interest in direct thermoelectric energy conversion [2–5] from waste heat to electricity has experienced a strong revival. Despite many promising features such as scalability and lack of moving parts, wide-scale adoption of thermoelectric materials is severely hampered by low energy-conversion efficiencies. The efficiency is measured by the dimensionless figure of merit $ZT = S^2\sigma T/\kappa$, where S denotes the Seebeck coefficient, and σ and κ are, respectively, electric and thermal conductivities [6]. This definition suggests several approaches to optimizing ZT [3]: for example, enhancing Seebeck coefficient and electronic conductivity via electronic band-structure engineering [7–9], and/or suppressing thermal conduction through phonon engineering [10–12]. However, this approach is often complicated by competing relationships; for example, increasing the electronic conductivity by introducing free carriers comes at the cost of an increased electronic thermal conductivity [5]. Despite these challenges the state-of-the-art ZT has continued to steadily increase (recently reaching as high as 2.6 [13]), with many improvements enabled by advances in modern nanotechnology and quantum design [2,3].

Since their emergence in the early 1980s [14,15], superlattices have attracted considerable attention as candidates for enhanced thermoelectric design. Through hybridization of two disparate materials, superlattices provide a viable approach to capitalizing on the signature properties of both constituent materials. For example, GaAs/AlAs superlattices [16–22] can be replacements for AlGaAs alloys in various electronic and optoelectronic devices, on account of greater carrier mobility and shallower dopant binding energies [23]. Recently interest in superlattices has been further renewed [24], stemming from studies of the thermoelectric performance of semiconductor quantum wells [25]. Several new superlattice materials exhibit promise for thermoelectrics, such as Si/Ge [22,26–32] and Bi_2Te_3/Sb_2Te_3 [33–34], in the latter of which the thermal conductivities are suppressed the most in the literature in comparison to parent materials.

Although engineered superlattices have offered a new avenue of phonon engineering and control over phonon propagation, to date several outstanding questions remain to be answered regarding the nature of phonon conduction on these ordered materials. Initial experimental measurements reported significant reduction of thermal conductivity by superlattice structuring, which was widely attributed to an interfacial Kapitza resistance [17,18,26]. Therefore, as the superlattice period decreases, the increasing interface density should result in reduced thermal conductivity. While this was supported by early numerical solutions to the Boltzmann equation [19], these deviate from more recent theoretical analyses [35] and simulations [30,36,37], which suggest that a minimum conductivity appears at a critical superlattice period. Despite several decades of analysis, a consistent picture of lattice thermal transport in superlattices is yet lacking. For example, Simkin and Mahan predict that the minima in the thermal conductivity appear when the period is close to the phonon mean free paths [35,36], while others predict that the minimum occurs at ultrashort periods [37]. Moreover, it is still unclear whether phonon transport on superlattices is ballistic and/or coherent [38]. Also it was not until this year that such minima were observed experimentally, and attributed to a crossover between coherent and incoherent transport [39].

Meanwhile, with continually increasing experimental capabilities at the nanoscale, the fabrication and characterization of low-dimensional materials has been attracting growing attention [24,40,41]. The synthesis and characterization of two-dimensional (2D) materials such as graphene [42], boron nitride [43], and kindred materials (e.g., the family of transition metal dichalcogenides [41]) has garnered substantial attention. Of particular interest is the recent successful fabrication of two-dimensional graphene and boron nitride composites

*Corresponding author: ertekin@illinois.edu

[44], which has further spurred a series of numerical studies [45,37,46]; recently even ordered 2D graphene/boron nitride (G/h-BN) superlattices [47] have been successfully fabricated. Although they share a honeycomb structure, graphene and boron nitride have distinct electronic structures, opening new possibilities for next-generation (opto-) electronics [47]. Nonetheless, their thermal properties are not well characterized thus far. Despite their similar atomic masses and lattice constants, boron nitride exhibits ionic/covalent bonding, in contrast to the covalent sp^2-hybrid bonds in graphene, resulting in different bond strengths. Additionally, the lattice thermal conductivity of 2D materials is interesting in its own right, as it has also been suggested that the thermal conductivity of pure two-dimensional materials diverges logarithmically with increasing total size [48,49].

In this work, we use computational atomistic methods to study the phononics of two-dimensional graphene/boron nitride superlattices. While the thermal conductivity of thin-film and/or nanowire superlattices is often found to exhibit a minimum at a critical superlattice period [35], the potentially diverging thermal conductivity of two-dimensional materials with total length [48,49] introduces an intriguing twist. More work is needed to thoroughly understand how these phenomena play out in two-dimensional superlattices, as well as the underlying mechanisms. The plan for this paper is as follows. In Sec. II we describe the two main numerical methods used in our work: nonequilibrium molecular dynamics (NEMD) and lattice dynamics (LD). In Sec. III we present the results of the NEMD and identify relevant length scales governing phonon transport. In Sec. IV, descriptions of interface effects applicable to the different regimes are introduced; Sec. V presents an extension of our analysis to nonideal superlattices. In Sec. VI the key findings of our work are summarized.

II. SIMULATION METHODS AND MODEL STRUCTURES

For our analysis, we have implemented two simulation methods: nonequilibrium molecular dynamics (NEMD) and lattice dynamics (LD). For both, we employ Tersoff potentials [50] for both graphene and boron nitride. The harmonic portion of the empirical potential is extracted and used to generate the LD results. For both materials, we use the parametrization of Lindsay and Broido [51], which has been optimized for descriptions of thermal properties. Tersoff's mixing rules [50] are applied to describe the interactions between C and B/N atoms at the interface (Supplemental Material [52]). As depicted in Fig. 1(a), the computational supercells consist of superlattices of regularly spaced graphene/boron nitride (G/h-BN) segments separated by zigzag interfaces. Periodic boundary conditions are applied to all simulation cell boundaries in each case, and thermal conductivity is calculated in the direction perpendicular to the interfaces. The period P of the superlattice and the total superlattice length L are varied. Here and hereafter, P and L are integers indicating the number of unit cell building blocks in the superlattice, where a "unit cell" is defined in Fig. 1(a).

Within NEMD, we simulate phonon transport on G/h-BN using LAMMPS [53]. All structures are initially relaxed and then thermalized at 300 K for 0.1 ns with Nose-Hoover thermostats. After the equilibration period, the thermal conductivity of each superlattice is determined using the Ikeshoji-Hafskjold approach [54]. Two heat baths (each 200 unit cells long) are established at the beginning and middle of the computational domain, and G/h-BN superlattices are inserted in between [Fig. 1(a) shows half of such a domain]. A constant heat flux Q from the heat source to the sink is established in the simulation cell, resulting in a temperature profile ∇T as shown in Fig. 1(b). A time step of 0.1 fs and 3.35 Å thickness are used to determine thermal conductivity k via Fourier's law $Q = k\nabla T$.

To assess the impact of harmonic modulation (wave effects) on the thermal conductivity, we also use LD [55] as implemented within GULP [56]. We extract the harmonic fit to the empirical Tersoff potentials about the minimum, from which we obtain bond "spring constants" of 1148, 900, and 1275 N/m, for graphene, boron nitride, and interface bonds,

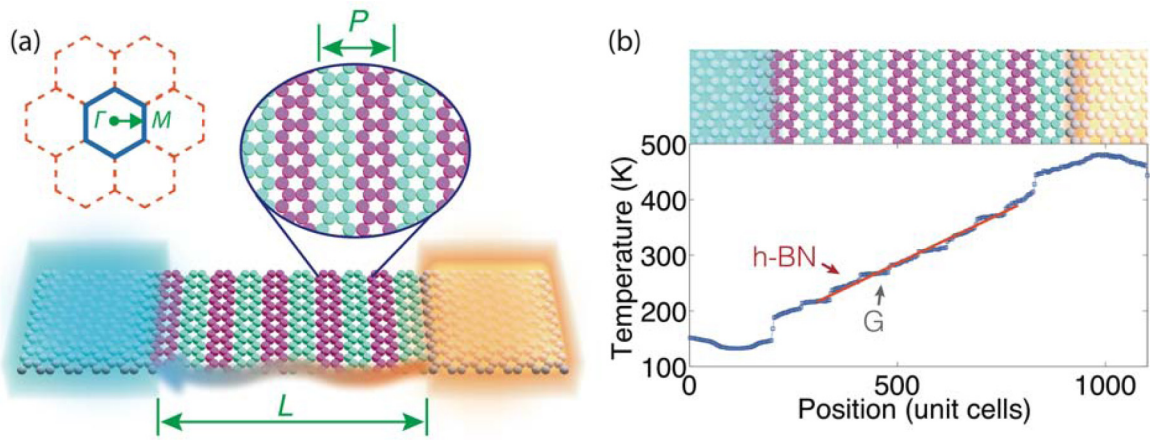

FIG. 1. (Color online) (a) Schematic of a five-period G/h-BN superlattice with $P = 2$ unit cells and $L = 5$ unit cells, where a unit cell has dimensions 0.246 and 0.426 nm parallel and perpendicular to the interface, respectively. Inset is reciprocal space and k locus used in this work; (b) Temperature profile of G/h-BN superlattice with $L = 700$ unit cells and $P = 140$ unit cells, which corresponds to local Knudsen number $\mathrm{Kn_{BN}} \approx 7$, $\mathrm{Kn_C} \approx 10$ and thus phonon flow features transition regime characteristics (note that the superlattice image on top is illustrative, the plotted data correspond to a larger period than depicted).

respectively. Using these spring constants within Simkin and Mahan's chain model approach [35] for each superlattice considered, the extended-zone representation of the lattice dispersion relationships can be determined. This analysis allows us to isolate the effects of phonon wave effects (arising from the superlattice periodicity) on the superlattice dispersion relationship.

III. NONEQUILIBRIUM MOLECULAR DYNAMICS AND LENGTH-SCALE ANALYSIS

A. Nonequilibrium molecular dynamics

The NEMD results of the thermal conductivity for G/h-BN superlattices with different total lengths L are shown as a function of the superlattice period P in Fig. 2(a). Total lengths of $L = 300, 500, 700$, and 1000 unit cells (as defined in Fig. 1) are considered. For each total length L the superlattice period P varies from ultrashort ($P = 2$ unit cells) to $P = L/2$ unit cells. From Fig. 2(a), it is clear that the overall superlattice thermal conductivities are notably reduced from those of the parent materials. For instance, according to our NEMD results for pure materials (not shown here explicitly), for length $L = 1000$ unit cells the thermal conductivity of graphene and boron nitride is $\sim$2000 and $\sim$1200 W/mK, respectively; by comparison the thermal conductivities of superlattices of the same length exhibit thermal conductivities of $\sim 400 - -600$ W/mK depending on the period. Additionally, the overall thermal conductivity in Fig. 2(a) increases steadily as the total length L of the superlattice increases, irrespective of the period P of the superlattice.

The most obvious feature in Fig. 2(a) is the minimum in the thermal conductivity that appears, independent of total superlattice length L, around a superlattice pitch P of 10–20 unit cells (4–8 nm). For fixed total length L, as the period grows, the calculated thermal conductivity initially decreases sharply for short-pitch superlattices, but then undergoes a relatively smooth increase. The emergence of a minimum thermal conductivity, substantially lower than that of the constituent materials, suggests that appropriately designed two-dimensional superlattices could be good candidates for low-thermal-conductivity applications, such as thermoelectric energy conversion. The presence of such minima in thin-film and nanowire superlattices has historically already received considerable attention in the literature. From different perspectives, several theories account for this nontrivial trend. For example, Simkin and Mahan [35] attribute it to the competition between wave and particle nature of the transport, while Jiang *et al.* [37] propose another possible explanation: diminution of wave tunneling versus the number of confined phonon modes. Venkatasubramanian [33] observed such behavior as well and interpreted it as a phonon localization phenomenon. It is interesting to note that these explanations sometimes arrive at different qualitative predictions, such as the characteristic length scale where the minimum occurs, and its dependence on carrier mean free paths and superlattice total lengths. In our case, the minima always occur at periods of $P = 10-20$ unit cells, independent of the total length L of the superlattices. Additionally, as shown in Fig. 2(b), normalizing the results by the minimum thermal conductivity collapses the data in Fig. 2(a) into a single curve, revealing a consistent scaling to the computed behavior.

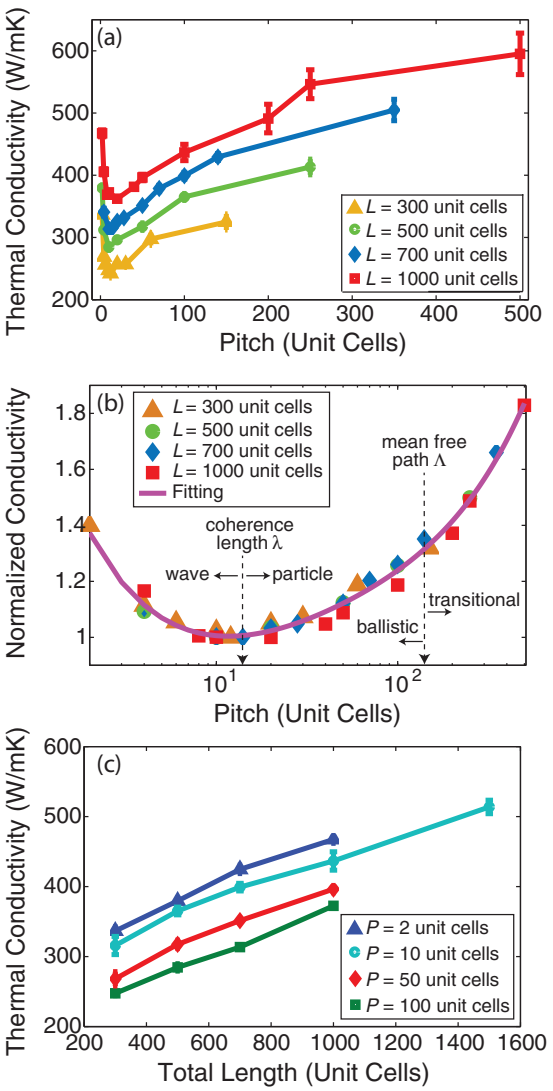

FIG. 2. (Color online) Thermal conductivity of ideal G/h-BN superlattices: (a) molecular dynamics results for varying P and L, minima occur at $P_c = 10-20$ unit cells; (b) thermal conductivity normalized by respective minima, showing a general valley trend and thus signifying universal critical length scales: coherence length $\lambda \approx 14 \pm 4$ unit cells and mean free path $\Lambda_G \approx 1400$ unit cells; (c) thermal conductivity versus total length L, where linear dependence indicates the ballistic nature of predominant carriers.

B. Relevant length scales

To understand the overall transport physics underlying the observed trends, in addition to the total length L and the superlattice period P, we identify several additional length scales. These are the phonon coherence length λ [19], and the local and global mean free paths $\Lambda_{l,g}$. The coherence length demarcates the length at which the wave nature of phonons become important relative to classical effects (particle nature) [57], while the mean free path weighs various collision mechanisms and describes the average phonon flight distance before scattering.

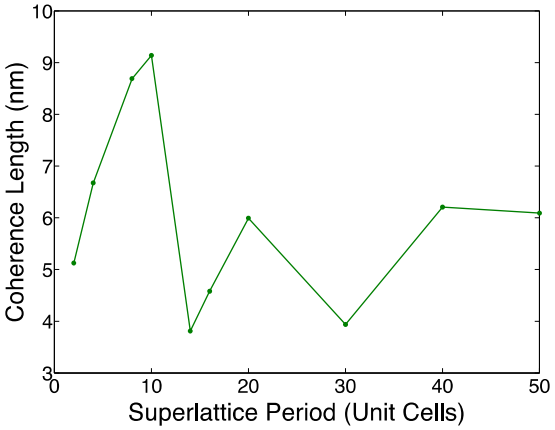

FIG. 3. (Color online) Calculated phononic coherence length λ as a function of the superlattice period P; the fluctuations are largely induced by Bose-Einstein weighting.

1. Phonon coherence lengths

We estimate the phonon coherence lengths as originally derived in Mehta [58] and later extended in Chen [19]. This approach only requires the phonon density of states as input, which we extract from our LD calculations (described later). We firstly weight the LD density of states $D(\omega)$ according to the Bose-Einstein distribution $N_{\mathrm{BE}}(\omega)$, and normalize such that $\int_0^{\omega_m} D(\omega)N_{\mathrm{BE}}(\omega)d\omega = 1$, where ω_m is the maximum frequency of all phonon modes. From Fourier analysis, the coherence time can be defined as

$$\tau = \int_0^{\omega_m} [D(\omega)N_{\mathrm{BE}}(\omega)]^2 d\omega, \tag{1}$$

which leads to the phonon coherence length as $\lambda = V_D\tau$, where V_D is the Debye velocity $V_D = (V_{\mathrm{LA}}^{-2} + V_{\mathrm{TA}}^{-2})^{-1/2}$ for two-dimensional phonon transport. The thus-computed coherence lengths for different periods P are plotted in Fig. 3, where Bose-Einstein weighting is responsible for some fluctuations in our numbers. The average value of coherence length, however, is found to be 6.02 ± 1.81 nm, which is equal to 14 ± 4 of our unit cells.

This calculated coherence length is marked on Fig. 2(b). Interestingly, we find that the coherence length precisely nests the NEMD conductivity minima. Thus, the minimum thermal conductivity occurs at a transition from wave-dominated to particle-dominated transport. To the left of the minimum ($P > \sim$6 nm), phonon transport is largely dominated by wave effects including constructive and destructive interferences arising from interfacial modulation; to the right of the minimum ($P > \sim$6 nm) phonon waves lose their coherence (i.e., phonon phase becomes unimportant) and transport is more particlelike.

2. Local and global mean free paths

To further elucidate the phonon transport within the particle regime to the right of the minimum, we have borrowed an idea from gas-kinetic theory. The phonon mean free path Λ gives rise to the dimensionless Knudsen number $\mathrm{Kn} = \Lambda/L_c$, which is the ratio of the mean free path to a characteristic length scale L_C. This ratio quantifies the degree of ballistic transport within a given system: The transport can be assumed collisionless when $\mathrm{Kn} > 10$, diffusive when $\mathrm{Kn} < 0.01$, and transitional in between [56]. In the discussion below, we consider the superlattice from two different perspectives: those of "local" and "global" phonons. In the local perspective, the superlattice is composed of a regular array of parent materials (graphene and boron nitride) with a well-defined interface separating the two; this perspective applies to local phonons that sense and can be scattered by interfaces. In the global perspective, we consider the superlattice as a new material altogether, with a unit cell given by one full G/h-BN period; this perspective applies to so-called global phonons of the superlattice itself that do not sense the interfacial modulation.

(a) Local Knudsen number Kn_l. We estimate mean free paths for pure graphene Λ_{C} and pure boron nitride Λ_{BN} using the kinetic definition of thermal conductivity $k \sim C_V v_g \Lambda$. Adopting the properties of boron nitride as given by the Ioffe Institute [59] (thermal capacity $C = 0.8\,\mathrm{J/g/K}$ and bulk modulus $B = 36\,\mathrm{GPa}$), and from its density $2.28\,\mathrm{g/cm^3}$, we obtain $C_V = 1.68 \times 10^6\,\mathrm{J/m^3\,K}$ and sound speed 4140.4 m/s. The above leads to an estimate of $\Lambda_{\mathrm{BN}} \approx 221.1$ nm. Similarly, for graphene we estimate $\Lambda_{\mathrm{C}} \approx 600$ nm, which is consistent with Pop *et al.* [48]. These estimates suggest that local transport within each graphene (h-BN) subdomain of the superlattice will be collisionless for pitches $P < 140\,(50)$ unit cells, using the threshold value for ballistic transport to be $\mathrm{Kn}_l = 10$. We have drawn a line at $P = 140$ unit cells on Fig. 2(b), which demarks this threshold for graphene within the particle regime: To the left $\mathrm{Kn}_l > 10$ and the transport should be ballistic; to the right $\mathrm{Kn}_l < 10$ and the flow becomes transitional. Note that in our simulations, the largest period P that we considered corresponds only to $\mathrm{Kn}_l = 6$ for graphene. Using a threshold of $\mathrm{Kn}_l = 0.01$, we note that P should be around 140 000 unit cells for diffusive transport, which is much larger than any system simulated here.

While true local ballistic transport would exhibit a constant temperature profile within each period in Fig. 1(b), any deviations from the ballistic regime should establish appropriate thermal gradients in our NEMD results. These are observed in Fig. 1(b) for the case of $P = 140$ unit cells (which corresponds to $\mathrm{Kn}_l = 10$ for graphene, and $\mathrm{Kn}_l = 7$ for boron nitride) as temperature gradients within each period (especially in the BN subdomains), indicating a phonon flow within the transitional flow regime.

(b) Global Knudsen number Kn_g. Turning now to global perspective, the definition of the global Knudsen number Kn_g is less straightforward since the mean free paths for the global phonons Λ_g are difficult to identify when the superlattices are viewed as new materials in and of themselves rather than two distinct materials separated by a sharp interface. The global phonons are those which are modes of the superlattice itself, and do not sense the interface as a distinct boundary between two materials. Given the difficulty to extract the mean free paths for the global phonons, we instead, as shown in Fig. 2(c), observe that the computed NEMD superlattice thermal conductivities scale nearly linearly with the total superlattice length L (independent of the period P). This observation suggests that the most dominant heat carriers—long-wavelength global phonons—are effectively transported ballistically for all of our simulated systems, so that $L \ll \Lambda_g$.

C. Length-scale analysis of NEMD results

The local and the global perspectives considered in tandem suggest that the dominant heat-carrying global phonons propagate heat ballistically without sensing the interfaces and determine the overall scale of the superlattice thermal conductivity (250–600 W/mK), which is substantially reduced from the parent materials (1200 W/mK for boron nitride, 5000 W/mK for graphene). On the other hand, the detailed features of the thermal conductivity in Figs. 2(a) and 2(b), including the emergence of the minimum, result from the fine-tuning by the localized phonons that do sense the interfaces. It is interesting to note that the ratio of global and local Knudsen numbers would quantify the impact of these localized phonons.

This perspective can help shed some light on the recent suggestions that the thermal conductivity of low-dimensional systems may diverge as the total length increases [48,49]. Such a divergence on two-dimensional suspended graphene has been recently reported, despite the presence of heat baths (pinning effects) [49]. Although the mechanism for such a divergence is still debated in the literature [60], it may be related to the relative weakness of anharmonic scattering in comparison to the contributions to the heat conduction by long-wavelength, low-frequency phonons that are activated as the system size increases. It may also be related to contributions from the high (diverging) density of states of the long-wavelength z-acoustic phonon modes that become activated as the sample size increases [61]. Although it is possible that for our systems the superlattice conductivity may diverge [we note that there is no discernible "leveling off" of the calculated conductivity in Fig. 2(c)], it is, however, very difficult for us to assess the possibility of a divergence numerically. As described above, convergence of the thermal conductivity (if it exists) for the pure materials would start emerging at $L \approx 140\,000$ unit cells (Kn ≈ 0.01), which requires large computational domains that are prohibitively large.

IV. DESCRIPTION OF INTERFACE EFFECTS

Having established the important length scales in our systems, we now take a more detailed look at the role of interfaces on the observed modulation of the thermal conductivity. In general, interfaces can play two critical roles: They are sources of inelastic scattering and they introduce harmonic modulation. The former has been well documented in literature and mostly studied via the Boltzmann equation [19], while the latter reflects changes to the phonon dispersion spectrum. We consider both effects here.

A. Interface effects in the wave region—lattice dynamics

To the left of the minimum in Fig. 2(b) where wave effects are important, the dominant role played by the interfaces are expected to be via modification to the lattice dispersion relationship induced by the periodic superlattice structure (wave interference effects). Lattice dynamics provides a viable vehicle to study ballistic transport, and our results are summarized in Fig. 4. Figure 4(a) shows the dispersion relationships calculated from LD for superlattices with two different periods: $P = 1$ and $P = 50$. Brillouin zone folding and wave interferences are reflected in these dispersion relationships. Once the dispersion relationships are established, the total thermal conductivity $k = L \sum_\chi k_\chi$ is calculated as a sum of the contributions over all modes χ. The modes in Fig. 4(a) are colored according to their spectral contribution to the total thermal conductivity given by $\kappa_\chi = v_g x^2 e^x (e^x - 1)^{-2}$ where $x = h\omega/kT$ and v_g is the group velocity $d\omega/dk$. A more detailed analysis showing the spectral contribution is presented in Fig. 4(b) for superlattices of pitch $P = 1$, 2, 4, 10, and 50. Here, the opening of band gaps can be easily identified, and the number of gaps increases with increasing pitch P.

The total thermal conductivity calculated from the sum is shown in the inset of Fig. 4(b), both when all modes are uniformly excited [Simkin and Mahan (MS) model] and according to the Bose-Einstein distribution (BE). In

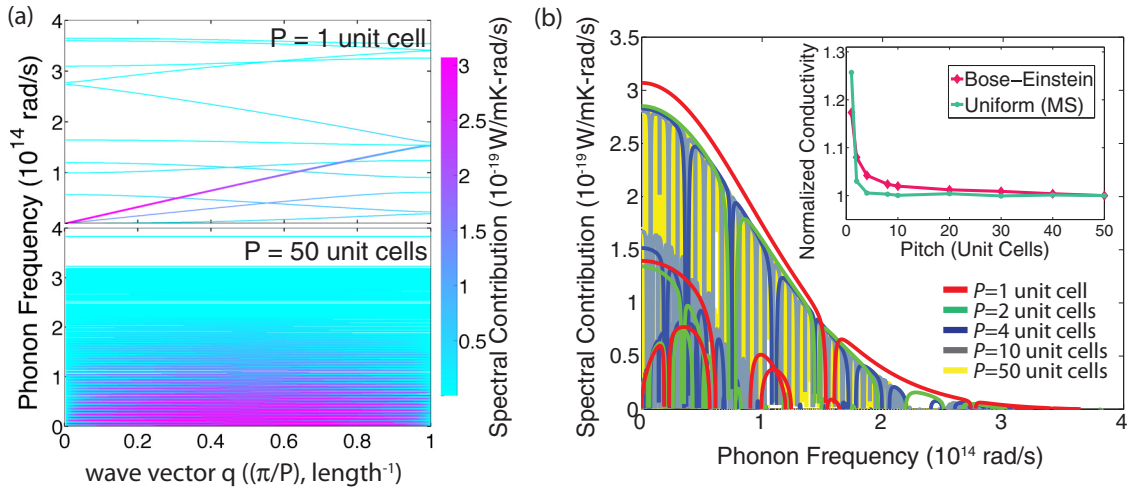

FIG. 4. (Color online) (a) Lattice dynamics calculation of modified dispersion curves of ideal G/h-BN and (b) spectral contribution to heat conductivity for varying periods. Increasing the pitch results in phonon band gaps and reduced group velocities, inducing a reduction of thermal conductivity, as shown in (b) inset (where MS means Simkin and Mahan's model [35]).

comparison to the NEMD results, the LD thermal conductivity initially drops as the pitch increases, but does not recover (no minimum is observed). Additionally, the overall reduction is sharper in the NEMD results in comparison to the LD results. Lattice dynamics therefore captures some portion, but not all, of the NEMD drop in the thermal conductivity of Figs. 2(a) and 2(b). The captured portion of the drop arises from the dominance of the wave nature of phonons and changes to the phononic band structure [35], ultimately causing spatial confinement of phonons and suppression of group velocity as originally described by Simkin and Mahan [35]. However, the initial reduction due to harmonic effects as captured by LD alone is not sufficient to explain the full reduction in Figs. 2(a) and 2(b) for ultrashort G/h-BN (the acoustic mismatch is quite low). To fully account for the pronounced reduction, nonlinear lattice dynamics [62] may be important in that nonlinearity can further flatten dispersion curves and enlarge band gaps [54].

B. Interface scattering in the particle region

The difference between the NEMD and LD results—namely the (lack of) recovery of the thermal conductivity beyond the minimum—implies the critical role of anharmonic processes not present in the LD in giving rise to the NEMD minimum in Figs. 2(a) and 2(b). To account for the recovery, anharmonic effects due to intrinsic umklapp damping [63] and interfacial scattering [64] (that are not captured by LD) are necessary. Both of these can be identified from the NEMD results in Fig. 1(b): the former from the thermal gradients within a given superlattice pitch, and the latter from the jumps at the interfaces. When the superlattice period grows, interfaces become sparser and interface scattering attenuates, which in turn leads to the increase of thermal conductivity [19,26,63].

In comparison to wave effects, interface scattering in the particle region is more straightforward and most applicable to long-pitch superlattices, where the interface represents a clearly defined border between two distinct materials. To assess its impact, we estimate the total superlattice thermal conductivity as the summed contribution of conductivity from both the local and global phonons as described in Sec. III B, so that $k_{SL} = k_l + k_g$. In this expression, the conductivity for the global phonons can be expressed from the kinetic description as $k_g(L) = C_g v_g L = \propto L$, provided that the total length $L \ll \Lambda_g$ which is valid for all of our simulated systems.

On the other hand, the contribution from the localized phonons $k_l(P)$ can be modeled by considering the graphene and boron nitride subdomains, and the interfaces between them, as resistors in series. Each superlattice of length L and period P consists of (L/P) integer units of graphene/boron nitride subdomains and two interfaces. The total resistance R_{TOT} of the superlattice is thus

$$R_{TOT} = \frac{L}{P}(R_G + R_{BN} + 2R_I), \tag{2}$$

where R_G, R_{BN}, and R_I are, respectively, the resistance of the graphene, boron nitride subdomains, and the interface. The resistivity is

$$\frac{R_{TOT}}{L} = \frac{1}{P}(R_G + R_{BN} + 2R_I), \tag{3}$$

and inverting gives the local phonon contribution to the conductivity,

$$k_l = \frac{1}{\frac{R_G}{P} + \frac{R_{BN}}{P} + \frac{2R_I}{P}}. \tag{4}$$

Since the thermal resistivity within the graphene (boron nitride) subdomain is $\rho_G = 1/k_G = R_G/(P/2)$ ($\rho_{BN} = 1/k_{BN} = R_{BN}/(P/2)$, then

$$k_l = 2\left(\frac{1}{k_G} + \frac{1}{k_{BN}} + \frac{4R_I}{P}\right)^{-1}. \tag{5}$$

In the near-ballistic transitional regime where $P \ll \Lambda_l$, from the kinetic definition of thermal conductivity we estimate $k_G \approx C_G v_G P$ and $k_{BN} \approx C_{BN} v_{BN} P$, so that finally

$$k_l = \frac{2P}{\left(\frac{1}{C_G v_G} + \frac{1}{C_{BN} v_{BN}} + 4R_I\right)} = \beta P. \tag{6}$$

Finally, we obtain $k_{SL} = k_g + k_l = \alpha L + \beta P$, so that in the particle region the thermal conductivity increases linearly with both total length L and pitch P. These linear relationships with period P and total length L are evident in Figs. 2(a) and 2(c), respectively. In Fig. 2(a), the observed near-linear relationship with P for large P beyond the minimum is thus consistent with the recovery of the thermal conductivity as a result of reduced interfacial scattering.

We note here that although increasing the pitch P will lead to an enhancement of thermal conductivity according to Eq. (6), the rate of increase should eventually slow down as the interfaces become sparser, the transport becomes diffuse, and phonon-phonon scattering within each constituent material intensifies. This corresponds to the violation of the limit $P \ll \Lambda_l$ adopted above. In Fig. 2(a), this leveling off for the largest $P > 200$ unit cells is somewhat apparent for the longer-length superlattices ($L = 700$, 1000 unit cells).

Using Eq. (6) and fitting to our NEMD results, we estimate an interfacial conductance of $1/R_I = 2.562 \times 10^9$ W/m^2 K. Therefore, in Fig. 5 we finally illustrate the thermal

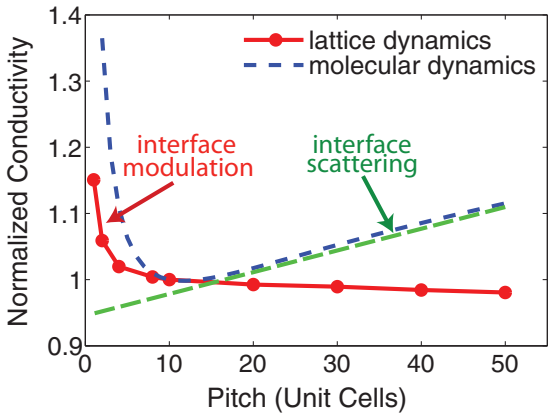

FIG. 5. (Color online) Comparison of normalized thermal conductivity calculated via NEMD and LD. The initial reduction of the thermal conductivity arises from wave effects, while reduced interfacial scattering is responsible for the recovery. The interface scattering model shown here is fitted to the NEMD results, using an interfacial conductance of $1/R_I = 2.562 \times 10^9$ /m^2 K.

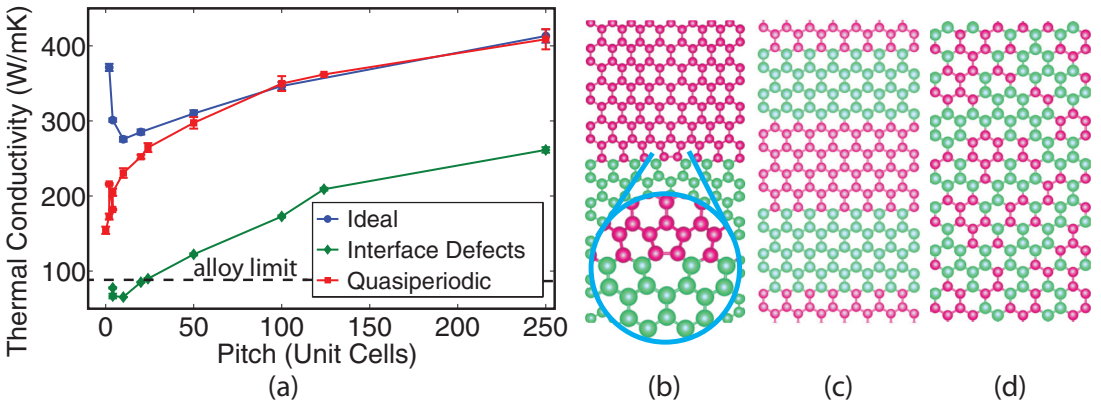

FIG. 6. (Color online) (a) Thermal conductivity of G/h-BN superlattices with (b) interface defects and (c) pseudoperiodicity. Thermal conductivity of pseudoperiodic G/h-BN increases monotonically with period P, ranging between (d) the alloy limit and ideal superlattices.

conductivity as the upshot of harmonic modulation effects (LD results, shown in red) and interfacial scattering (interface scattering model, shown in green). It is interesting to note that the combination of discreteness (dispersion) and nonlinearity can result in exotic effects such as discrete breathers and solitons on superlattices, which would be an intriguing direction for future study.

V. EXTENSION TO NONIDEAL SUPERLATTICES

Before concluding, it is important to point out that such thermal-conductivity minima seldom appear in published experimental work (except Ravichandaran *et al.* [39]), despite numerous theoretical and computational predictions. This is often attributed to the presence of additional scattering mechanisms such as defects at the interface (i.e., misfit dislocations in thin-film superlattices) that can mask the minimum. We have tested the robustness of the NEMD results in the presence of both interfacial defects and periodicity disorder (Fig. 6).

The green line in Fig. 6(a) shows the thermal conductivity when interfacial 7-5 defects are present. Due to the 2% lattice mismatch between graphene and boron nitride, these 7-5 "misfit dislocations" [see Fig. 6(b)] may be expected to form at interfaces [65]. The thermal conductivity of these incoherent superlattices is substantially reduced from the ideal superlattice (blue line); for example, the lattice thermal conductivity reduces more than 4.25 times at the minimum compared to the ideal case. It appears that the strain fields associated with the dislocations themselves introduce extraneous phonon scattering mechanisms and enhance interfacial resistance. Additionally, if such interfacial defects are present, the minimum (if it exists) will be difficult to resolve, giving way to a thermal conductivity that mainly increases with increasing period.

Additionally, within NEMD we also simulated "pseudoperiodic" superlattices, which exhibit a ± 1 atom layer random perturbation of the superlattice period [Fig. 6(c)]. As indicated by the red line in Fig. 6(a), slight disorder to the periodicity can effectively dissolve the minimum as well, probably via a mechanism closely related to Anderson localization [66]. Therefore, even if the interfaces are defect-free, imperfect periodicity also could cause the lattice thermal conductivity to appear to increase monotonically with period. Moreover, the thermal conductivity of these pseudoperiodic G/h-BN systems spans between the ideal and alloy limit, but never below.

Given the current challenges in the fabrication of such atomically sharp interfaces with perfect periodicity in low-dimensional materials, we predict that experimental measurement of such a thermal-conductivity minimum should be very difficult to achieve.

VI. CONCLUSIONS

In summary, using nonequilibrium molecular dynamics we observed a conductivity minimum of G/h-BN superlattices at a critical pitch, and interpreted it as the result of the interplay between lattice dispersion effects and interfacial scattering. For all of the systems considered here, the dominant transporting phonons are ballistic, long-wavelength carriers that set the overall scale of the thermal conductivity, which increases nearly linearly with total superlattice length. Meanwhile, localized phonon modes induce subtle changes in the thermal conductivity and produce the minima at a critical superlattice pitch. The superlattice period tunes finely the transport nature of phonon flows, spanning from dispersion dominated, through ballistic, to the transition regime. Interface modulation leads to phonon localization, but anharmonic effects play equally important roles on the superlattices consisting of acoustically akin materials. Interfaces have attracted intense attention in the past, and numerical results in this work demonstrate that thermal conductivity depends critically on interface topology. Additional interesting features remain to be explored: For instance, low-dimensional superlattices feature large surface areas well suited for functionalization which open additional tuning routes.

ACKNOWLEDGMENTS

We acknowledge fruitful discussions with Dinkar Nandwana and Sanjiv Sinha. This work is supported by the National Science Foundation, through Grant No. CBET-1250192. Computational resources: This research is part of the Blue Waters sustained-petascale computing project, which is supported by the National Science Foundation (Awards No. OCI-0725070 and No. ACI-1238993) and the state of Illinois. Blue Waters is

a joint effort of the University of Illinois at Urbana-Champaign and its National Center for Supercomputing Applications. Additional resources were provided by (i) the Extreme Science and Engineering Discovery Environment (XSEDE), which is supported by National Science Foundation Grant No. ACI-1053575, and (ii) the Illinois Campus Computing Cluster.

[1] S. Chu and A. Majumdar, Nature **488**, 294 (2012).
[2] M. S. Dresselhaus, G. Chen, M. Y. Tang, R. G. Yang, H. Lee, D. Z. Wang, Z. F. Ren, J. P. Fleurial, and P. Gogna, Adv. Mater. **19**, 1043 (2007).
[3] J. P. Heremans, M. S. Dresselhaus, L. E. Bell, and D. T. Morelli, Nat. Nanotechnol. **8**, 471 (2013).
[4] G. D. Mahan and J. O. Sofo, Proc. Natl. Acad. Sci. USA **93**, 7436 (1996).
[5] G. J. Snyder and E. S. Toberer, Nat. Mater. **7**, 105 (2008).
[6] G. S. Nolas, J. Sharp, and H. J. Goldsmid, *Thermoelectrics: Basic Principles and New Materials Developments* (Springer, Berlin, 2001).
[7] S. Ishiwata, Y. Shiomi, J. S. Lee, M. S. Bahramy, T. Suzuki, M. Uchida, R. Arita, Y. Taguchi, and Y. Tokura, Nat. Mater. **12**, 512 (2013).
[8] J. P. Heremans, V. Jovovic, E. S. Toberer, A. Saramat, K. Kurosaki, A. Charoenphakdee, S. Yamanaka, and G. J. Snyder, Science **321**, 554 (2008).
[9] Y. Pei, H. Wang, and G. J. Snyder, Adv. Mater. **24**, 6125 (2012).
[10] G. Chen, T. Zeng, T. Borca-Tasciuc, and D. Song, Mater. Sci. Eng. A **292**, 155 (2000).
[11] A. A. Balandin, J. Nanosci. Nanotechnol. **5**, 1015 (2005).
[12] D. J. Voneshen, K. Refson, E. Borissenko, M. Krisch, A. Bosak, A. Piovano, E. Cemal, M. Enderle, M. J. Gutmann, M. Hoesch, M. Roger, L. Gannon, A. T. Boothroyd, S. Uthayakumar, D. G. Porter, and J. P. Goff, Nat. Mater. **12**, 1028 (2013).
[13] L. D. Zhao, S. H. Lo, Y. Zhang, H. Sun, G. Tan, C. Uher, C. Wolverton, V. P. Dravid, and M. G. Kanatzidis, Nature **508**, 373 (2014).
[14] A. Y. Cho, Appl. Phys. Lett. **19**, 467 (1971).
[15] L. Esaki and L. L. Chang, Phys. Rev. Lett. **33**, 495 (1974).
[16] C. Colvard, T. A. Gant, M. V. Klein, R. Merlin, R. Fischer, H. Morkoc, and A. C. Gossard, Phys. Rev. B **31**, 2080 (1985).
[17] T. Yao, Appl. Phys. Lett. **51**, 1798 (1987).
[18] G. Chen, A. Verma, and J. S. Smith, Appl. Phys. Lett. **67**, 3554 (1995).
[19] G. Chen, J. Heat Trans. **119**, 220 (1997); **121**, 945 (1999); Phys. Rev. B **57**, 14958 (1998).
[20] W. S. Capinski, H. J. Maris, T. Ruf, M. Cardona, K. Ploog, and D. S. Katzer, Phys. Rev. B **59**, 8105 (1999).
[21] V. Narayanamurti, H. L. Störmer, M. A. Chin, A. C. Gossard, and W. Wiegmann, Phys. Rev. Lett. **43**, 2012 (1979).
[22] S. Tamura, Y. Tanaka, and H. J. Maris, Phys. Rev. B **60**, 2627 (1999).
[23] R. Dingle, H. L. Stormer, A. C. Gossard, and W. Wiegmann, Appl. Phys. Lett. **33**, 665 (1978).
[24] D. G. Cahill, W. K. Ford, K. E. Goodson, G. D. Mahan, A. Majumdar, H. J. Maris, R. Merlin, and S. R. Phillpot, J. Appl. Phys. **93**, 793 (2003); D. G. Cahill, P. V. Braun, G. Chen, D. R. Clarke, S. Fan, K. E. Goodson, P. Keblinski, W. P. King, G. D. Mahan, A. Majumdar, H. J. Maris, S. R. Phillpot, E. Pop, and L. Shi, Appl. Phys. Rev. **1**, 011305 (2014).
[25] L. D. Hicks and M. S. Dresselhaus, Phys. Rev. B **47**, 12727 (1993); L. D. Hicks, T. C. Harman, and M. S. Dresselhaus, Appl. Phys. Lett. **63**, 3230 (1993).
[26] S. M. Lee, D. G. Cahill, and R. Venkatasubramanian, Appl. Phys. Lett. **70**, 2957 (1997).
[27] T. Borca-Tasciuc, W. Liu, J. Liu, T. Zeng, D. W. Song, C. D. Moore, G. Chen, K. L. Wang, and M. S. Goorsky, Superlattices Microstruct. **28**, 199 (2000).
[28] S. T. Huxtable, A. R. Abramson, C. L. Tien, A. Majumdar, C. LaBounty, X. Fan, G. Zeng, J. E. Bowers, A. Shakouri, and E. T. Croke, Appl. Phys. Lett. **80**, 1737 (2002).
[29] V. Samvedi and V. Tomar, Nanotechnology **20**, 365701 (2009).
[30] M. Hu and D. Poulikakos, Nano Lett. **12**, 5487 (2012).
[31] J. Garg and G. Chen, Phys. Rev. B **87**, 140302 (2013).
[32] I. Savić, D. Donadio, F. Gygi, and G. Galli, Appl. Phys. Lett. **102**, 073113 (2013).
[33] R. Venkatasubramanian, Phys. Rev. B **61**, 3091 (2000).
[34] M. N. Touzelbaev, P. Zhou, R. Venkatasubramanian, and K. E. Goodson, J. Appl. Phys. **90**, 763 (2001).
[35] M. V. Simkin and G. D. Mahan, Phys. Rev. Lett. **84**, 927 (2000).
[36] Y. Chen, D. Li, J. R. Lukes, Z. Ni, and M. Chen, Phys. Rev. B **72**, 174302 (2005).
[37] J. Jiang, J. Wang, and B. Wang, Appl. Phys. Lett. **99**, 043109 (2011).
[38] M. N. Luckyanova, J. Garg, K. Esfarjani, A. Jandl, M. T. Bulsara, A. J. Schmidt, A. J. Minnich, S. Chen, M. S. Dresselhaus, Z. Ren, E. A. Fitzgerald, and G. Chen, Science **338**, 936 (2012).
[39] J. Ravichandran, A. K. Yadav, R. Cheaito, P. B. Rossen, A. Soukiassian, S. J. Suresha, J. C. Duda, B. M. Foley, C. H. Lee, Y. Zhu, A. W. Lichtenberger, J. E. Moore, D. A. Muller, D. G. Schlom, P. E. Hopkins, A. Majumdar, R. Ramesh, and M. A. Zurbuchen, Nat. Mater. **13**, 168 (2014).
[40] V. Nicolosi, M. Chhowalla, M. G. Kanatzidis, M. S. Strano, and J. N. Coleman, Science **340**, 1226419 (2013).
[41] K. S. Novoselov, D. Jiang, F. Schedin, T. J. Booth, V. V. Khotkevich, S. V. Morozov, and A. K. Geim, Proc. Natl. Acad. Sci. USA **102**, 10451 (2005).
[42] K. S. Novoselov, V. I. Fal'ko, L. Colombo, P. R. Gellert, M. G. Schwab, and K. Kim, Nature **490**, 192 (2012).
[43] K. Watanabe, T. Taniguchi, and H. Kanda, Nat. Mater. **3**, 404 (2004).
[44] L. Ci, L. Song, C. Jin, D. Jariwala, D. Wu, Y. Li, A. Srivastava, Z. F. Wang, K. Storr, L. Balicas, F. Liu, and P. M. Ajayan, Nat. Mater. **9**, 430 (2010).
[45] H. Sevincli, W. Li, N. Mingo, G. Cuniberti, and S. Roche, Phys. Rev. B **84**, 205444 (2011).
[46] A. Kinaci, J. B. Haskins, C. Sevik, and T. Cagin, Phys. Rev. B **86**, 115410 (2012).
[47] Z. Liu, L. Ma, G. Shi, W. Zhou, Y. Gong, S. Lei, X. Yang, J. Zhang, J. Yu, K. P. Hackenberg, A. Babakhani, J. C. Idrobo, R. Vajtai, J. Lou, and P. M. Ajayan, Nat. Nanotechnol. **8**, 119 (2013).
[48] E. Pop, V. Varshney, and A. K. Roy, MRS Bull. **37**, 1273 (2012).

[49] X. Xu, L. F. C. Pereira, Y. Wang, J. Wu, K. Zhang, X. Zhao, S. Bae, C. T. Bui, R. Xie, J. T. L. Thong, B. H. Hong, K. P. Loh, D. Donadio, B. Li, and B. Özyilmaz, Nat. Commun. **5**, 1 (2014).
[50] J. Tersoff, Phys. Rev. B **37**, 6991 (1988); **39**, 5566 (1989).
[51] L. Lindsay and D. A. Broido, Phys. Rev. B **81**, 205441 (2010); **84**, 155421 (2011).
[52] See Supplemental Material at http://link.aps.org/supplemental/10.1103/PhysRevB.90.195209 for a summary of the parameters of the empirical potentials.
[53] S. Plimpton, J. Comput. Phys. **117**, 1 (1995); http://lammps.sandia.gov.
[54] T. Ikeshoji and B. Hafskjold, Mol. Phys. **81**, 251 (1994).
[55] M. Born and K. Huang, *Dynamical Theory of Crystal Lattices* (Clarendon Press, Oxford, 1954).
[56] J. D. Gale and A. L. Rohl, Mol. Simulat. **29**, 291 (2003).
[57] G. Chen, *Nanoscale Energy Transport and Conversion: A Parallel Treatment of Electrons, Molecules, Phonons, and Photons* (Oxford University Press, Oxford, 2005).
[58] C. L. Mehta, Il Nuovo Cimento **28**, 401 (1963).
[59] See http://www.ioffe.ru/SVA/NSM/Semicond/BN/thermal.html, and references therein.
[60] A. Dhar, Adv. Phys. **57**, 457 (2008).
[61] A. A. Balandin, Nat. Mater. **10**, 569 (2011).
[62] H. Bilz, H. Büttner, A. Bussmann-Holder, W. Kress, and U. Schröder, Phys. Rev. Lett. **48**, 264 (1982).
[63] R. E. Peierls, *Quantum Theory of Solids* (Clarendon Press, Oxford, 2001).
[64] B. Yang and G. Chen, Phys. Rev. B **67**, 195311 (2003).
[65] D. Nandwana and E. Ertekin (unpublished).
[66] P. W. Anderson, Phys. Rev. **109**, 1492 (1958).